

Highlights

- Neural trajectories in the hippocampus exhibited greater variability during a working memory (WM) task compared to those in the entorhinal cortex and amygdala regions.
- The distance of neural trajectories between encoding and retrieval states in the hippocampus was memory-load dependent during a WM task.
- Hippocampal neural trajectories fluctuated between the encoding and retrieval states in a task-dependent manner during both baseline and sharp-wave ripple (SWR) periods.
- Hippocampal neural trajectories shifted from encoding to retrieval states during SWR period.

Hippocampal neural fluctuations between memory encoding and retrieval states during a working memory task in humans

Yusuke Watanabe^{a,*}, Yuji Ikegaya^{b,c,d}, Takufumi Yanagisawa^{a,e}

^a*Institute for Advanced Cocreation studies, Osaka University, 2-2 Yamadaoka, Suita, 565-0871, Osaka, Japan*

^b*Graduate School of Pharmaceutical Sciences, The University of Tokyo, 7-3-1 Hongo, Tokyo, 113-0033, Japan*

^c*Institute for AI and Beyond, The University of Tokyo, 7-3-1 Hongo, Tokyo, 113-0033, Japan*

^d*Center for Information and Neural Networks, National Institute of Information and Communications Technology, 1-4 Yamadaoka, Suita City, 565-0871, Osaka, Japan*

^e*Department of Neurosurgery, Osaka University Graduate School of Medicine, 2-2 Yamadaoka, Osaka, 565-0871, Japan*

Abstract

Working memory (WM) forms a crucial foundation for a multitude of cognitive functions, yet the complex neural mechanisms underlying its operation are not fully understood. More specifically, while the hippocampus and sharp-wave ripple complexes (SWRs) — rapid, coordinated neuronal activities within the hippocampus — are known to play roles in memory consolidation and retrieval, their contribution to WM tasks remains somewhat ambiguous. Our current research suggests that the multiunit activity patterns in the hippocampus operate in synergy with SWRs, exhibiting distinguishable dynamics during WM tasks. We conducted a comprehensive analysis of a dataset derived from intracranial electroencephalogram recordings of the medial temporal lobe (MTL) from nine epilepsy patients performing an eight-second Sternberg task. We utilized Gaussian-process factor analysis to identify low-dimensional neuronal representations, or ‘trajectories,’ within the MTL regions during the WM task. Our data showed that the neuronal trajectory varied most significantly in the hippocampus compared to the entorhinal cortex and amygdala. Furthermore, variations in the trajectories between the encoding and retrieval phases were dependent on memory load. Notably, hippocampal trajectories oscillated during the retrieval phase, showcasing task-dependent transitions between encoding and retrieval states, including baseline and SWR periods. These oscillations transitioned from encoding to retrieval states aligned with SWRs. Thus, our findings emphasize the vital role of the hippocampus in carrying out WM tasks and propose a compelling hypothesis for future investigation: the functional state of the hippocampus transitions from encoding to retrieval during SWRs.

Keywords: working memory, WM, memory load, hippocampus, sharp-wave ripples, SWR, humans

Working memory (WM) plays a crucial role in everyday life, and its neural underpinnings remain an area of ongoing research. The hippocampus, notably integral to memory, continues to be a primary focus of this investigation [1] [2] [3] [4] [5] [6] [7] [8] [9]. Gaining insights into the role of the hippocampus in working memory is vital to deepening our understanding of cognitive processes, hence fostering the progression of cognitive training and interventions.

Current evidence suggests a transient, synchronized oscillation, referred to as sharp-wave ripple (SWR) [10],

is linked with several cognitive functions, such as memory replay [11] [12] [13] [14] [15], memory consolidation [16] [17] [18] [19], memory recall [20] [21] [22], and neural plasticity [23] [24]. This evidence indicates the likelihood that SWR could be a critical component of hippocampal processing, contributing to working memory performance. However, research investigating the effects of SWRs on working memory remains sparse [25], and is largely limited to rodent models participating in navigation tasks where the timing of memory acquisition and recall is not explicitly distinguished.

Recent studies indicate that hippocampal neurons exhibit low-dimensional representations during WM

*Corresponding author. Tel: +81-6-6879-3652

tasks. Notably, the firing patterns of place cells [26] [27] [28] [29] [30], located in the hippocampus, are observed to be encompassed within a dynamic, nonlinear three-dimensional hyperbolic geometry in rodents [31]. Moreover, grid cells in the entorhinal cortex (EC)—the dominant pathway to the hippocampus [32] [33] [34]—displayed toroidal topology during exploration [35]. Unfortunately, these investigations are confined to spatial navigation tasks in rodents, thus imposing limitations on the temporal resolution of WM tasks. The applicability of these findings to human subjects and their generalization beyond navigation tasks remains to be established.

Given these considerations, the current study aims to validate the hypothesis that hippocampal neurons exhibit distinctive representations in low-dimensional spaces, designated as ‘neural trajectory,’ during WM tasks, most prominently within SWR periods. To evaluate this claim, we employed a dataset of patients performing an eight-second Sternberg task with high temporal resolution (1 s for fixation, 2 s for encoding, 3 s for maintenance, and 2 s for retrieval), while their intracranial electroencephalography signals (iEEG) within the medial temporal lobe (MTL) were being monitored [36]. To investigate low-dimensional neural trajectories, we employed Gaussian-process factor analysis (GPFA), a method renowned for analyzing neural population dynamics [37].

1. Methods

1.1. Dataset

A publicly available dataset [36] was used, which consists of nine epilepsy patients performing a modified Sternberg task. This task involves four phases: fixation (1s), encoding (2s), maintenance (3s), and retrieval (2s) [36]. During the encoding phase, participants were exposed to four, six, or eight alphabet letters, referred to as the set size. Subsequently, they had to decide whether a probe letter presented during the retrieval phase was previously displayed (the correct choice for the Match IN task) or not (the correct choice for the Mismatch OUT task). iEEG signals were recorded at a sampling rate of 32 kHz, within a frequency range of 0.5–5,000 Hz, using depth electrodes implanted in the medial temporal lobe (MTL) regions:

the anterior head of the left and the right hippocampus (AHL and AHR), the posterior body of the hippocampus (PHL and PHR), the entorhinal cortex (ECL and ECR), and the amygdala (AL and AR), as illustrated in Figure 1A and Table 1. The iEEG signals were subsequently downsampled to a rate of 2 kHz. Correlations among variables such as set size and correct rate were investigated (Figure ??S1). The timings of multiunit spikes were determined by a spike sorting algorithm [38] using the Combinato package (<https://github.com/jniediek/combinato>) (Figure 1C).

1.2. Calculation of neural trajectories using GPFA

Neural trajectories, also termed ‘factors’ (Figure 1D), in the hippocampus, EC, and amygdala (Figure 1D), were computed using GPFA [37] applied to the multiunit activity data for each session. GPFA was performed with the elephant package (<https://elephant.readthedocs.io/en/latest/reference/gpfa.html>). The bin size was set to 50 ms, with no overlaps. Each factor was z-normalized across all sessions. The Euclidean distance from the origin (O) was then calculated (Figure 1E).

For each trajectory within a region, for instance, AHL, *geometric medians* (i.e., g_F for fixation, g_E for encoding, g_M for maintenance, and g_R for retrieval phase) were determined by calculating the median coordinates of the trajectory during the four phases (Figure 1D). An optimal dimensionality for GPFA was identified as three using the elbow method, which was derived by investigating the log-likelihood values through a three-fold cross-validation approach (Figure 2B).

1.3. Identifying SWR candidates from hippocampal regions

Potential SWR events within the hippocampus were detected using a widely accepted method [39]. LFP signals from a region of interest (ROI), such as AHL, were re-referenced by subtracting an averaged signal from locations outside the ROI (e.g., AHR, PHL, PHR, ECL, ECR, AL, and AR) (see Figure 1A). The re-referenced LFP signals were then filtered with a ripple-band filter (80–140 Hz) to identify SWR candidates (=SWR⁺ candidates) (see Figure 1B). SWR detection was conducted using a published tool (https://github.com/Eden-Kramer-Lab/ripple_detection) [40], with the bandpass range adjusted to 80–140 Hz for humans

[21] [22], different from the original 150–250 Hz range typically applied to rodents.

Control events for SWR^+ candidates, labeled as SWR^- candidates, were identified by randomly shuffling the timestamps of SWR^+ candidates across all trials and subjects. The resulting $\text{SWR}^+/\text{SWR}^-$ candidates were then subjected to visual inspection, as shown in Figure 1.

1.4. Defining SWRs from putative hippocampal CA1 regions

SWRs were distinguished from SWR candidates in presumptive CA1 regions. Initially, these regions were defined as follows: $\text{SWR}^+/\text{SWR}^-$ candidates in the hippocampus were projected into a two-dimensional space based on overlapping spike counts per unit employing a supervised method using UMAP (Uniform Manifold Approximation and Projection) [41] (Figure 4A). Clustering validation was performed by computing the silhouette score [42] from clustered samples (Table 2). Regions in the hippocampus, which scored above 0.6 on average across sessions (75th percentile) (Figure 4B), were characterized as presumed CA1 regions, identifying five electrode positions from five patients (Table 3).

$\text{SWR}^+/\text{SWR}^-$ candidates in the assumed CA1 regions were classified as $\text{SWR}^+/\text{SWR}^-$, thus relinquishing their candidate status. The duration and ripple band peak amplitude of SWRs were observed to follow log-normal distributions (Figure 4C & E). Each time period of SWR was partitioned relative to the time from the SWR center into pre- (at -800 to -300 ms from SWR center), mid- (at -250 to $+250$ ms), and post-SWR (at $+300$ to $+800$ ms) times.

1.5. Statistical evaluation

The Brunner–Munzel test and the Kruskal–Wallis test were performed using the SciPy package in Python [43]. Correlational analysis was performed by determining the rank of the observed correlation coefficient in its associated set-size-shuffled surrogate using a custom Python script. The bootstrap test was implemented using an in-house Python script.

2. Results

2.1. iEEG recording and neural trajectory in MTL regions during a Sternberg task

We leveraged a publicly available dataset for this analysis [36]. This dataset encompasses LFP signals (Figure 1A) from MTL regions (Table 1) during a modified Sternberg task execution. We identified SWR^+ candidates from LFP signals filtered through the 80–140 Hz ripple band (Figure 1B), originating across all hippocampal regions (refer to Methods). Correspondingly, SWR^- candidates were defined at identical timestamps) but shuffled across different trials (Figure 1). The dataset included multiunit spikes (Figure 1C) identified via a spike sorting algorithm [38]. By employing GPFA [37], and using the 50-ms binned multiunit activity with no overlaps, we determined the neural trajectories (or factors) of MTL regions by session and region (Figure 1D). We normalized each factor by session and region for instance, session #2 in AHL of subject #1. Subsequently, we calculated the Euclidean distance from the origin (O) (Figure 1E).

2.2. Hippocampal neural trajectory correlation with a Sternberg task

Figure 2A illustrates the cloud of median neural trajectories of 50 trials within the three main factor spaces. We determined the optimal embedding dimension for the GPFA model to be three, using the elbow method (Figure 2B). The trajectory distance from the origin (O) (represented as $\|g_F\|$, $\|g_E\|$, $\|g_M\|$, and $\|g_R\|$) in the hippocampus exceeded corresponding distances in the EC and amygdala (Figures 2C and D).¹

Similarly, we computed the distances between the geometric medians of four phases, namely $\|g_{FGE}\|$, $\|g_{FGM}\|$, $\|g_{FGR}\|$, $\|g_{EGM}\|$, $\|g_{EGR}\|$, and $\|g_{MGR}\|$. The results indicated that the hippocampus displayed larger distances between phases than both the EC and amygdala.²

¹Hippocampus: Distance = 1.11 [1.01], median [IQR], $n = 195,681$ timepoints; EC: Distance = 0.94 [1.10], median [IQR], $n = 133,761$ timepoints; Amygdala: Distance = 0.78 [0.88], median [IQR], $n = 165,281$ timepoints.

²Hippocampus: Distance = 0.60 [0.70], median [IQR], $n = 8,772$ combinations; EC: Distance = 0.28 [0.52], median [IQR], $n = 5,017$ combinations ($p < 0.01$; Brunner–Munzel test); Amygdala: Distance = 0.24 [0.42], median [IQR], $n = 7,466$ combinations ($p < 0.01$; Brunner–Munzel test).

2.3. Memory load-dependent neural trajectory distance between encoding and retrieval states in the hippocampus

In terms of memory load in the Stenberg task, we identified a negative correlation between the correct rate of trials and set size (the number of letters to encode) (Figure 3A).³ Similarly, a positive correlation was observed between the response time and set size (Figure 3B).⁴

Furthermore, we found a positive correlation between set size and the trajectory distance between the encoding and retrieval phases ($\log_{10}||g_{EGR}||$) (Figure 3C).⁵ However, distances between other combinations of phases did not display statistically significant correlations (Figures 3D and S2).

2.4. Detection of hippocampal SWR from putative CA1 regions

For precision improvement in recording sites and SWR detection, we estimated the electrode placements in the CA1 regions of the hippocampus using distinct multiunit spike patterns during the SWR events. SWR⁺/SWR⁻ candidates from every session and hippocampal region were embedded in a two-dimensional space using UMAP (Figure 4A).⁶ We used the silhouette score as a metric for quality of clustering (Figure 4B and Table 2). Recording sites with an average silhouette score exceeding 0.6 across all sessions were identified as putative CA1 regions.⁷ (Tables 2 and 3). We identified five putative CA1 regions, four of which were not

labeled as seizure onset zones (Table 1).

Subsequently, SWR⁺/SWR⁻ candidates within these putative CA1 regions were labeled as SWR⁺ and SWR⁻, respectively⁸ (Table 3). Both SWR⁺ and SWR⁻ exhibited the same duration⁹ (Figure 4C) due to their definitions, and followed a log-distribution. We observed an augmentation in SWR⁺ incidence during the initial 400 ms of the retrieval phase¹⁰ (Figure 4D). The peak ripple band amplitude of SWR⁺ outpaced SWR⁻ and followed a log-normal distribution (Figure 4E).¹¹

2.5. Transient changes in hippocampal neural trajectory during SWR

We computed the distance of the trajectory from the origin (*O*) during SWR events in both the encoding and retrieval phases (Figure 5A). Observing the increase in distance during SWR as shown in Figure 5A, we differentiated each SWR into three stages: pre-, mid-, and post-SWR. Therefore, the distances from *O* during those SWR periods are identified as $||pre-eSWR^+||$, $||mid-eSWR^+||$ among others.

$||mid-eSWR^+||$ ¹² was greater than $||pre-eSWR^+||$ ¹³, and $||mid-rSWR^+||$ ¹⁴ was larger than $||pre-rSWR^+||$ in both Match IN and Mismatch OUT tasks.¹⁵

2.6. Visualization of hippocampal neural trajectory during SWR in two-dimensional spaces

Following our observations of neural trajectory 'jumping' during SWR (Figure 5), we visualized the three-dimensional trajectories of pre-, mid-, and post-SWR events during the encoding and retrieval phases (Figure 6), the distance between which was found to be

³Correct rate: set size four (0.99 ± 0.11 , mean \pm SD; $n = 333$ trials) vs. set size six (0.93 ± 0.26 ; $n = 278$ trials; $p < 0.001$, Brunner–Munzel test with Bonferroni correction) and set size eight (0.87 ± 0.34 ; $n = 275$ trials; $p < 0.05$; Brunner–Munzel test with Bonferroni correction). Overall, $p < 0.001$ for Kruskal–Wallis test; correlation coefficient = -0.20, $p < 0.001$.

⁴Response time: set size four (1.26 ± 0.45 s; $n = 333$ trials) vs. set size six (1.53 ± 0.91 s; $n = 278$ trials) and set size eight (1.66 ± 0.80 s; $n = 275$ trials). All comparisons $p < 0.001$, Brunner–Munzel test with Bonferroni correction; $p < 0.001$ for Kruskal–Wallis test; correlation coefficient = 0.22, $p < 0.001$.

⁵Correlation between set size and $\log_{10}||g_{EGR}||$: correlation coefficient = 0.05, $p < 0.001$. Specific values: $||g_{EGR}|| = 0.54$ [0.70] for set size four, $n = 447$; $||g_{EGR}|| = 0.58$ [0.66] for set size six, $n = 381$; $||g_{EGR}|| = 0.61$ [0.63] for set size eight, $n = 395$.

⁶Consider the AHL in session #1 of subject #1, for illustration purposes.

⁷The identified regions were: AHL of subject #1, AHR of subject #3, PHL of subject #4, AHL of subject #6, and AHR of subject #9.

⁸These definitions led to equal counts for both categories: SWR⁺ ($n = 1,170$) and SWR⁻ ($n = 1,170$).

⁹These definitions led to equal durations for both categories: SWR⁺ (93.0 [65.4] ms) and SWR⁻ (93.0 [65.4] ms).

¹⁰SWR⁺ increased against the bootstrap sample; 95th percentile = 0.42 [Hz]; $p < 0.05$.

¹¹SWR⁺ (3.05 [0.85] SD of baseline, median [IQR]; $n = 1,170$) vs. SWR⁻ (2.37 [0.33] SD of baseline, median [IQR]; $n = 1,170$; $p < 0.001$; Brunner–Munzel test).

¹²1.25 [1.30], median [IQR], $n = 1,281$, in Match IN task; 1.12 [1.35], median [IQR], $n = 1,163$, in Mismatch OUT task

¹³1.08 [1.07], median [IQR], $n = 1,149$, in Match IN task; 0.90 [1.12], median [IQR], $n = 1,088$, in Mismatch OUT task

¹⁴1.32 [1.24], median [IQR], $n = 935$, in Match IN task; 1.15 [1.26], median [IQR], $n = 891$, in Mismatch OUT task

¹⁵1.19 [0.96], median [IQR], $n = 673$, in Match IN task; 0.94 [0.88], median [IQR], $n = 664$, in Mismatch OUT task

memory-load dependent (Figure 3).

To provide two-dimensional visualization, we linearly aligned peri-SWR trajectories by assigning \mathbf{g}_E at the origin (0, 0) and \mathbf{g}_R at ($\|\mathbf{g}_{EGR}\|$, 0). Post this, we rotated these aligned trajectories around the \mathbf{g}_{EGR} axis (the x-axis). Thus, the distances from the origin in the original three-dimensional spaces are preserved in the two-dimensional equivalent.

The scatter plot within these two-dimensional spaces reveals characteristic distributions of peri-SWR trajectories based on phases and task types. For instance, one can observe that the magnitude of $\|\text{mid-eSWR}^+\|$ surpasses that of $\|\text{pre-eSWR}^+\|$ (Figure 6B), consistent with our earlier findings (Figure 5).

2.7. Fluctuations of hippocampal neural trajectories between encoding and retrieval states

Next, we examined trajectory *directions* in relation to \mathbf{g}_{EGR} . The directions of SWRs were defined by the neural trajectory at -250 ms and $+250$ ms from their center, i.e., \mathbf{eSWR}^+ .

We calculated the density of $\mathbf{eSWR}^+ \cdot \mathbf{g}_{EGR}$, $\mathbf{rSWR}^+ \cdot \mathbf{g}_{EGR}$, and $\mathbf{eSWR}^- \cdot \mathbf{rSWR}^-$ (Figures 7A–D). $\mathbf{rSWR}^- \cdot \mathbf{g}_{EGR}$ displayed a biphasic distribution.

By taking the difference between the distribution of $\mathbf{rSWR}^+ \cdot \mathbf{g}_{EGR}$ (Figures 7A and B) and that of $\mathbf{rSWR}^- \cdot \mathbf{g}_{EGR}$ (Figures 7C and D), we computed the contributions of SWR (Figures 7E and F), which revealed a shift in the direction of \mathbf{g}_{EGR} (Figures 7E and F: *red rectangles*).

Moreover, exclusively in the Mismatch OUT task, $\mathbf{eSWR}^+ \cdot \mathbf{rSWR}^+$ was less than $\mathbf{eSWR}^- \cdot \mathbf{rSWR}^-$ (baseline periods) (Figure 7F: *pink circles*). In simpler terms, eSWR and rSWR pointed in the opposite direction only in the Mismatch OUT task but not in the Match IN task (Figure 7E: *pink circles*).

3. Discussion

4. Discussion

This study hypothesized that within low-dimensional spaces during a working memory (WM) task in humans, hippocampal neurons form unique trajectories, particularly during sharp-wave ripple (SWR) periods. Initially, the multiunit spikes in medial temporal lobe (MTL) regions were projected onto three-dimensional spaces

during a Sternberg task using Gaussian Process Factor Analysis (GPFA) (Figure 1D–E and Figure 2A). The distance of the trajectory across WM phases ($\|\mathbf{g}_{FGE}\|$, $\|\mathbf{g}_{FGM}\|$, $\|\mathbf{g}_{FGR}\|$, $\|\mathbf{g}_{EGM}\|$, $\|\mathbf{g}_{EGR}\|$, and $\|\mathbf{g}_{MGR}\|$) was notably larger in the hippocampus than in the EC and amygdala (Figure 2E), indicating dynamic neural activity in the hippocampus during the WM task. Further, in the hippocampus, the trajectory distance between the encoding and retrieval phases ($\|\mathbf{g}_{FGE}\|$) exhibited a positive correlation with memory load (Figure 3C–D), reflecting WM processing. The hippocampal neural trajectory was found to increase transiently during SWRs (Figure 5). Finally, the hippocampal neural trajectory switched between encoding and retrieval states, moving from encoding to retrieval during SWR events (Figure 7). These findings not only explain various facets of hippocampal neural activity during a WM task in humans but also offer new insights into how SWRs influence the switch in neural states.

We found that the distance of the neural trajectory across the phases was greater in the hippocampus compared to that in the EC and amygdala, even when considering the distance from O in these regions (Figure 2C–E). This supports the involvement of the hippocampus in the WM task, aligning with previous reports of hippocampal persistent firing during the maintenance phase [3] [4] [5] [6]. However, when we applied GPFA to multiunit activity during a 1-second level resolution of the WM task, we observed that the neural trajectory in low-dimensional space showed a memory-load dependency between the encoding and retrieval phases, symbolized as $\|\mathbf{g}_{EGR}\|$ (Figure 3). These findings corroborate the association of the hippocampus with WM processing.

Our analysis was confined to putative CA1 regions (Figure 4), which was bolstered by several factors. This specific focus stems from established observations that SWRs synchronize with spike bursts of interneurons and pyramidal neurons [44] [45] [46] [47], potentially within a $50 \mu\text{m}$ radius of the recording site [48]. We further identified an increased incidence of SWRs during the first 0–400 ms of the retrieval phase (Figure 4D). This finding harmonizes with previous reports of heightened SWR occurrence preceding spontaneous verbal recall [21] [22], supporting our results under a triggered retrieval condition. The observed log-normal distributions of both SWR duration and ripple band peak ampli-

tude in this study (Figure 4C & E) is in accordance with the consensus in this field [39]. As a result, our decision to restrict recording sites to putative CA1 regions likely contributed to enhancing the accuracy of SWR detection. However, the increase in trajectory distance from *O* during SWRs (Figure 5) might have been skewed towards higher values due to channel selection. However, this potential bias does not substantially challenge our primary findings.

Interestingly, during the retrieval phase, the trajectory directions oscillated between encoding and retrieval states during both baseline and SWR periods (Figure 7C & D). Moreover, the balance of this oscillation shifted from encoding to retrieval state during SWR events (Figure 7E & F). These results are consistent with previous reports on the role of SWR in memory retrieval [21] [22]. Our findings highlight a new understanding, suggesting that SWRs occur when the hippocampal representation transitions from encoding to retrieval states. Therefore, these results reveal novel aspects of hippocampal representations, including (i) neuronal oscillation between encoding and retrieval states during a WM task and (ii) SWR serving as a trigger for changing neural states.

Furthermore, our study uncovered WM-task type-specific differences between encoding- and retrieval-SWRs (Figure 7E–F). Notably, opposing movements of encoding-SWR (eSWR) and retrieval-SWR (rSWR) were not observed in the Match IN task but were apparent in the Mismatch OUT task. These observations can be explained by the memory engram theory [49]. Particularly, the Match In task provided participants with previously presented letters, contrastingly, the Mismatch OUT task introduced a new letter not present in the encoding phase. These interpretations underscore the significant role of SWR in human cognitive processes.

In conclusion, the present investigation demonstrated that hippocampal activity oscillates between encoding and retrieval states during a WM task and uniquely transitions from encoding to retrieval during SWR incidents. These findings provide meaningful insight into the neural counterparts and functionality of working memory in the hippocampus.

References

- [1] W. B. Scoville, B. Milner, LOSS OF RECENT MEMORY AFTER BILATERAL HIPPOCAMPAL LESIONS, *Journal of Neurology, Neurosurgery, and Psychiatry* 20 (1) (1957) 11–21. URL <https://www.ncbi.nlm.nih.gov/pmc/articles/PMC497229/>
- [2] L. R. Squire, The Legacy of Patient H.M. for Neuroscience, *Neuron* 61 (1) (2009) 6–9. doi:10.1016/j.neuron.2008.12.023. URL <https://www.ncbi.nlm.nih.gov/pmc/articles/PMC2649674/>
- [3] E. Boran, T. Fedele, P. Klaver, P. Hilfiker, L. Stieglitz, T. Grunwald, J. Sarnthein, Persistent hippocampal neural firing and hippocampal-cortical coupling predict verbal working memory load, *Science Advances* 5 (3) (2019) eaav3687. doi:10.1126/sciadv.aav3687. URL <https://www.science.org/doi/10.1126/sciadv.aav3687>
- [4] J. Kamiński, S. Sullivan, J. M. Chung, I. B. Ross, A. N. Mamelak, U. Rutishauser, Persistently active neurons in human medial frontal and medial temporal lobe support working memory, *Nature Neuroscience* 20 (4) (2017) 590–601, number: 4 Publisher: Nature Publishing Group. doi:10.1038/nn.4509. URL <https://www.nature.com/articles/nn.4509>
- [5] S. Kornblith, R. Q. Quiroga, C. Koch, I. Fried, F. Mormann, Persistent Single-Neuron Activity during Working Memory in the Human Medial Temporal Lobe, *Current Biology* 27 (7) (2017) 1026–1032, publisher: Elsevier. doi:10.1016/j.cub.2017.02.013. URL [https://www.cell.com/current-biology/abstract/S0960-9822\(17\)30149-5](https://www.cell.com/current-biology/abstract/S0960-9822(17)30149-5)
- [6] M. C. M. Faraut, A. A. Carlson, S. Sullivan, O. Tudusciuc, I. Ross, C. M. Reed, J. M. Chung, A. N. Mamelak, U. Rutishauser, Dataset of human medial temporal lobe single neuron activity during declarative memory encoding and recognition, *Scientific Data* 5 (1) (2018) 180010, number: 1 Publisher: Nature Publishing Group. doi:10.1038/sdata.2018.10. URL <https://www.nature.com/articles/sdata201810>
- [7] A. A. Borders, C. Ranganath, A. P. Yonelinas, The hippocampus supports high-precision binding in visual working memory, *Hippocampus* 32 (3) (2022) 217–230. doi:10.1002/hipo.23401.
- [8] J. Li, D. Cao, S. Yu, X. Xiao, L. Imbach, L. Stieglitz, J. Sarnthein, T. Jiang, Functional specialization and interaction in the amygdala-hippocampus circuit during working memory processing, *Nature Communications* 14 (1) (2023) 2921, number: 1 Publisher: Nature Publishing Group. doi:10.1038/s41467-023-38571-w. URL <https://www.nature.com/articles/s41467-023-38571-w>
- [9] V. Dimakopoulos, P. Mégevand, L. H. Stieglitz, L. Imbach, J. Sarnthein, Information flows from hippocampus to auditory cortex during replay of verbal working memory items, *eLife* 11 (2022) e78677, publisher: eLife Sciences Publications, Ltd. doi:10.7554/eLife.78677. URL <https://doi.org/10.7554/eLife.78677>
- [10] G. Buzsáki, Hippocampal sharp wave-ripple: A cognitive biomarker for episodic memory and planning, *Hippocampus* 25 (10) (2015) 1073–1188, eprint: <https://onlinelibrary.wiley.com/doi/pdf/10.1002/hipo.22488>. doi:<https://doi.org/10.1002/hipo.22488>.

- URL <https://onlinelibrary.wiley.com/doi/abs/10.1002/hipo.22488>
- [11] M. A. Wilson, B. L. McNaughton, Reactivation of hippocampal ensemble memories during sleep, *Science* (New York, N.Y.) 265 (5172) (1994) 676–679. doi:10.1126/science.8036517.
 - [12] Z. Nádasdy, H. Hirase, A. Czurkó, J. Csicsvari, G. Buzsáki, Replay and Time Compression of Recurring Spike Sequences in the Hippocampus, *Journal of Neuroscience* 19 (21) (1999) 9497–9507, publisher: Society for Neuroscience Section: ARTICLE. doi:10.1523/JNEUROSCI.19-21-09497.1999. URL <https://www.jneurosci.org/content/19/21/9497>
 - [13] A. K. Lee, M. A. Wilson, Memory of sequential experience in the hippocampus during slow wave sleep, *Neuron* 36 (6) (2002) 1183–1194. doi:10.1016/s0896-6273(02)01096-6.
 - [14] K. Diba, G. Buzsáki, Forward and reverse hippocampal place-cell sequences during ripples, *Nature Neuroscience* 10 (10) (2007) 1241–1242, number: 10 Publisher: Nature Publishing Group. doi:10.1038/nn1961. URL <https://www.nature.com/articles/nn1961>
 - [15] T. J. Davidson, F. Kloosterman, M. A. Wilson, Hippocampal replay of extended experience, *Neuron* 63 (4) (2009) 497–507. doi:10.1016/j.neuron.2009.07.027.
 - [16] G. Girardeau, K. Benchenane, S. I. Wiener, G. Buzsáki, M. B. Zugaro, Selective suppression of hippocampal ripples impairs spatial memory, *Nature Neuroscience* 12 (10) (2009) 1222–1223. doi:10.1038/nn.2384. URL <http://www.nature.com/articles/nn.2384>
 - [17] V. Ego-Stengel, M. A. Wilson, Disruption of ripple-associated hippocampal activity during rest impairs spatial learning in the rat, *Hippocampus* 20 (1) (2010) 1–10. doi:10.1002/hipo.20707.
 - [18] A. Fernández-Ruiz, A. Oliva, E. Fermino de Oliveira, F. Rocha-Almeida, D. Tingley, G. Buzsáki, Long-duration hippocampal sharp wave ripples improve memory, *Science* (New York, N.Y.) 364 (6445) (2019) 1082–1086. doi:10.1126/science.aax0758. URL <https://www.ncbi.nlm.nih.gov/pmc/articles/PMC6693581/>
 - [19] J. Kim, A. Joshi, L. Frank, K. Ganguly, Cortical–hippocampal coupling during manifold exploration in motor cortex, *Nature* (2022) 1–8 Publisher: Nature Publishing Group. doi:10.1038/s41586-022-05533-z. URL <https://www.nature.com/articles/s41586-022-05533-z>
 - [20] C.-T. Wu, D. Haggerty, C. Kemere, D. Ji, Hippocampal awake replay in fear memory retrieval, *Nature Neuroscience* 20 (4) (2017) 571–580. doi:10.1038/nn.4507.
 - [21] Y. Norman, E. M. Yeagle, S. Khuvis, M. Harel, A. D. Mehta, R. Malach, Hippocampal sharp-wave ripples linked to visual episodic recollection in humans, *Science* 365 (6454) (2019) eaax1030. doi:10.1126/science.aax1030. URL <https://www.sciencemag.org/lookup/doi/10.1126/science.aax1030>
 - [22] Y. Norman, O. Raccach, S. Liu, J. Parvizi, R. Malach, Hippocampal ripples and their coordinated dialogue with the default mode network during recent and remote recollection, *Neuron* 109 (17) (2021) 2767–2780.e5, publisher: Elsevier. doi:10.1016/j.neuron.2021.06.020. URL [https://www.cell.com/neuron/abstract/S0896-6273\(21\)00461-X](https://www.cell.com/neuron/abstract/S0896-6273(21)00461-X)
 - [23] C. J. Behrens, L. P. van den Boom, L. de Hoz, A. Friedman, U. Heinemann, Induction of sharp wave–ripple complexes in vitro and reorganization of hippocampal networks, *Nature Neuroscience* 8 (11) (2005) 1560–1567, number: 11 Publisher: Nature Publishing Group. doi:10.1038/nn1571. URL <https://www.nature.com/articles/nn1571>
 - [24] H. Norimoto, K. Makino, M. Gao, Y. Shikano, K. Okamoto, T. Ishikawa, T. Sasaki, H. Hioki, S. Fujisawa, Y. Ikegaya, Hippocampal ripples down-regulate synapses, *Science* (New York, N.Y.) 359 (6383) (2018) 1524–1527. doi:10.1126/science.aao0702.
 - [25] S. P. Jadhav, C. Kemere, P. W. German, L. M. Frank, Awake Hippocampal Sharp-Wave Ripples Support Spatial Memory, *Science* 336 (6087) (2012) 1454–1458, publisher: American Association for the Advancement of Science. doi:10.1126/science.1217230. URL <https://www.science.org/doi/abs/10.1126/science.1217230>
 - [26] J. O’Keefe, J. Dostrovsky, The hippocampus as a spatial map: Preliminary evidence from unit activity in the freely-moving rat, *Brain Research* 34 (1971) 171–175, place: Netherlands Publisher: Elsevier Science. doi:10.1016/0006-8993(71)90358-1.
 - [27] J. O’Keefe, Place units in the hippocampus of the freely moving rat, *Experimental Neurology* 51 (1) (1976) 78–109. doi:10.1016/0014-4886(76)90055-8. URL <https://www.sciencedirect.com/science/article/pii/0014488676900558>
 - [28] A. D. Ekstrom, M. J. Kahana, J. B. Caplan, T. A. Fields, E. A. Isham, E. L. Newman, I. Fried, Cellular networks underlying human spatial navigation, *Nature* 425 (6954) (2003) 184–188, number: 6954 Publisher: Nature Publishing Group. doi:10.1038/nature01964. URL <https://www.nature.com/articles/nature01964>
 - [29] K. B. Kjelstrup, T. Solstad, V. H. Brun, T. Hafting, S. Leutgeb, M. P. Witter, E. I. Moser, M.-B. Moser, Finite Scale of Spatial Representation in the Hippocampus, *Science* 321 (5885) (2008) 140–143, publisher: American Association for the Advancement of Science. doi:10.1126/science.1157086. URL <https://www.science.org/doi/abs/10.1126/science.1157086>
 - [30] C. D. Harvey, F. Collman, D. A. Dombeck, D. W. Tank, Intracellular dynamics of hippocampal place cells during virtual navigation, *Nature* 461 (7266) (2009) 941–946, number: 7266 Publisher: Nature Publishing Group. doi:10.1038/nature08499. URL <https://www.nature.com/articles/nature08499>
 - [31] H. Zhang, P. D. Rich, A. K. Lee, T. O. Sharpee, Hippocampal spatial representations exhibit a hyperbolic geometry that expands with experience, *Nature Neuroscience* (Dec. 2022). doi:10.1038/s41593-022-01212-4. URL <https://www.nature.com/articles/s41593-022-01212-4>
 - [32] P. A. Naber, F. H. Lopes da Silva, M. P. Witter, Reciprocal connections between the entorhinal cortex and hippocampal fields CA1 and the subiculum are in reg-

- ister with the projections from CA1 to the subiculum, *Hippocampus* 11 (2) (2001) 99–104, eprint: <https://onlinelibrary.wiley.com/doi/pdf/10.1002/hipo.1028>. doi:10.1002/hipo.1028. URL <https://onlinelibrary.wiley.com/doi/abs/10.1002/hipo.1028>
- [33] N. M. van Strien, N. L. M. Cappaert, M. P. Witter, The anatomy of memory: an interactive overview of the parahippocampal–hippocampal network, *Nature Reviews Neuroscience* 10 (4) (2009) 272–282, number: 4 Publisher: Nature Publishing Group. doi:10.1038/nrn2614. URL <https://www.nature.com/articles/nrn2614>
- [34] B. A. Strange, M. P. Witter, E. S. Lein, E. I. Moser, Functional organization of the hippocampal longitudinal axis, *Nature Reviews Neuroscience* 15 (10) (2014) 655–669, number: 10 Publisher: Nature Publishing Group. doi:10.1038/nrn3785. URL <https://www.nature.com/articles/nrn3785>
- [35] R. J. Gardner, E. Hermansen, M. Pachitariu, Y. Burak, N. A. Baas, B. A. Dunn, M.-B. Moser, E. I. Moser, Toroidal topology of population activity in grid cells, *Nature* 602 (7895) (2022) 123–128, number: 7895 Publisher: Nature Publishing Group. doi:10.1038/s41586-021-04268-7. URL <https://www.nature.com/articles/s41586-021-04268-7>
- [36] E. Boran, T. Fedele, A. Steiner, P. Hilfiker, L. Stieglitz, T. Grunwald, J. Sarnthein, Dataset of human medial temporal lobe neurons, scalp and intracranial EEG during a verbal working memory task, *Scientific Data* 7 (1) (2020) 30, number: 1 Publisher: Nature Publishing Group. doi:10.1038/s41597-020-0364-3. URL <https://www.nature.com/articles/s41597-020-0364-3>
- [37] B. M. Yu, J. P. Cunningham, G. Santhanam, S. I. Ryu, K. V. Shenoy, M. Sahani, Gaussian-Process Factor Analysis for Low-Dimensional Single-Trial Analysis of Neural Population Activity, *Journal of Neurophysiology* 102 (1) (2009) 614–635. doi:10.1152/jn.90941.2008. URL <https://www.ncbi.nlm.nih.gov/pmc/articles/PMC2712272/>
- [38] J. Niediek, J. Boström, C. E. Elger, F. Mormann, Reliable Analysis of Single-Unit Recordings from the Human Brain under Noisy Conditions: Tracking Neurons over Hours, *PLOS ONE* 11 (12) (2016) e0166598, publisher: Public Library of Science. doi:10.1371/journal.pone.0166598. URL <https://journals.plos.org/plosone/article?id=10.1371/journal.pone.0166598>
- [39] A. A. Liu, S. Henin, S. Abbaspoor, A. Bragin, E. A. Buffalo, J. S. Farrell, D. J. Foster, L. M. Frank, T. Gedankien, J. Gotman, J. A. Guidera, K. L. Hoffman, J. Jacobs, M. J. Kahana, L. Li, Z. Liao, J. J. Lin, A. Losonczy, R. Malach, M. A. van der Meer, K. McClain, B. L. McNaughton, Y. Norman, A. Navas-Olive, L. M. de la Prida, J. W. Rueckemann, J. J. Sakon, I. Skelin, I. Soltesz, B. P. Staresina, S. A. Weiss, M. A. Wilson, K. A. Zaghloul, M. Zugaro, G. Buzsáki, A consensus statement on detection of hippocampal sharp wave ripples and differentiation from other fast oscillations, *Nature Communications* 13 (1) (2022) 6000, number: 1 Publisher: Nature Publishing Group. doi:10.1038/s41467-022-33536-x. URL <https://www.nature.com/articles/s41467-022-33536-x>
- [40] K. Kay, M. Sosa, J. E. Chung, M. P. Karlsson, M. C. Larkin, L. M. Frank, A hippocampal network for spatial coding during immobility and sleep, *Nature* 531 (7593) (2016) 185–190. doi:10.1038/nature17144.
- [41] L. McInnes, J. Healy, N. Saul, L. Großberger, UMAP: Uniform Manifold Approximation and Projection, *Journal of Open Source Software* 3 (29) (2018) 861. doi:10.21105/joss.00861. URL <https://joss.theoj.org/papers/10.21105/joss.00861>
- [42] P. J. Rousseeuw, Silhouettes: A graphical aid to the interpretation and validation of cluster analysis, *Journal of Computational and Applied Mathematics* 20 (1987) 53–65. doi:10.1016/0377-0427(87)90125-7. URL <https://www.sciencedirect.com/science/article/pii/0377042787901257>
- [43] P. Virtanen, R. Gommers, T. E. Oliphant, M. Haberland, T. Reddy, D. Cournapeau, E. Burovski, P. Peterson, W. Weckesser, J. Bright, S. J. van der Walt, M. Brett, J. Wilson, K. J. Millman, N. Mayorov, A. R. J. Nelson, E. Jones, R. Kern, E. Larson, C. J. Carey, Polat, Y. Feng, E. W. Moore, J. VanderPlas, D. Laxalde, J. Perktold, R. Cimrman, I. Henriksen, E. A. Quintero, C. R. Harris, A. M. Archibald, A. H. Ribeiro, F. Pedregosa, P. van Mulbregt, SciPy 1.0 Contributors, SciPy 1.0: fundamental algorithms for scientific computing in Python, *Nature Methods* 17 (2020) 261–272, aDS Bibcode: 2020NatMe..17..261V. doi:10.1038/s41592-019-0686-2. URL <https://ui.adsabs.harvard.edu/abs/2020NatMe..17..261V>
- [44] G. Buzsáki, Two-stage model of memory trace formation: a role for "noisy" brain states, *Neuroscience* 31 (3) (1989) 551–570. doi:10.1016/0306-4522(89)90423-5.
- [45] M. L. V. Quyen, A. Bragin, R. Staba, B. Crépon, C. L. Wilson, J. Engel, Cell Type-Specific Firing during Ripple Oscillations in the Hippocampal Formation of Humans, *Journal of Neuroscience* 28 (24) (2008) 6104–6110, publisher: Society for Neuroscience Section: Brief Communications. doi:10.1523/JNEUROSCI.0437-08.2008. URL <https://www.jneurosci.org/content/28/24/6104>
- [46] S. Royer, B. V. Zemelman, A. Losonczy, J. Kim, F. Chance, J. C. Magee, G. Buzsáki, Control of timing, rate and bursts of hippocampal place cells by dendritic and somatic inhibition, *Nature Neuroscience* 15 (5) (2012) 769–775, number: 5 Publisher: Nature Publishing Group. doi:10.1038/nn.3077. URL <https://www.nature.com/articles/nn.3077>
- [47] N. Hájos, M. R. Karlócai, B. Németh, I. Ulbert, H. Monyer, G. Szabó, F. Erdélyi, T. F. Freund, A. I. Gulyás, Input-output features of anatomically identified CA3 neurons during hippocampal sharp wave/ripple oscillation in vitro, *The Journal of Neuroscience: The Official Journal of the Society for Neuroscience* 33 (28) (2013) 11677–11691. doi:10.1523/JNEUROSCI.5729-12.2013.
- [48] E. W. Schomburg, C. A. Anastassiou, G. Buzsáki, C. Koch, The Spiking Component of Oscillatory Extracellular Potentials in the Rat Hippocampus, *The Journal of Neuroscience* 32 (34) (2012) 11798–11811. doi:10.1523/JNEUROSCI.0656-12.2012.

URL <https://www.ncbi.nlm.nih.gov/pmc/articles/PMC3459239/>

- [49] X. Liu, S. Ramirez, P. T. Pang, C. B. Puryear, A. Govindarajan, K. Deisseroth, S. Tonegawa, Optogenetic stimulation of a hippocampal engram activates fear memory recall, *Nature* 484 (7394) (2012) 381–385, number: 7394 Publisher: Nature Publishing Group. doi:10.1038/nature11028.
URL <https://www.nature.com/articles/nature11028>

Contributors

Y.W. and T.Y. conceptualized the study; Y.W. performed the data analysis; Y.W. and T.Y. wrote the original draft; and all authors reviewed the final manuscript.

Acknowledgments

This research was funded by a grant from the Exploratory Research for Advanced Technology (JPM-JER1801).

Declaration of Interests

The authors declare that they have no competing interests.

Data and code availability

The data is available on G-Node (<https://doi.gin.g-node.org/10.12751/g-node.d76994/>). The source code is available on GitHub (<https://github.com/yanagisawa-lab/hippocampal-neural-fluctuation-during-a-WM-task-in-humans>).

Inclusion and Diversity Statement

We support inclusive, diverse, and equitable conduct of research.

Declaration of Generative AI in Scientific Writing

The authors employed ChatGPT, provided by OpenAI, for enhancing the manuscript's English language quality. After incorporating the suggested improvements, the authors meticulously revised the content. Ultimate responsibility for the final content of this publication rests entirely with the authors.

Tables

| Subject ID | of sessions | AHL | AHR | PHL | PHR | ECL | ECR | AL | AR | SOZ |
|------------|-------------|-----|-----|-----|-----|-----|-----|----|----|----------------------|
| 1 | 4 | o | x | o | o | o | x | o | x | "AHR, LR" |
| 2 | 7 | o | o | o | o | o | o | o | o | "AHR, PHR" |
| 3 | 3 | o | o | o | o | o | o | o | x | "AHL, PHL" |
| 4 | 2 | o | o | o | o | o | o | o | o | "AHL, AHR, PHL, PHR" |
| 5 | 3 | o | x | x | o | x | x | o | x | DRR |
| 6 | 6 | o | o | o | o | o | o | o | o | "AHL, PHL, ECL, AL" |
| 7 | 4 | o | o | o | o | o | o | o | o | "AHR, PHR" |
| 8 | 5 | o | o | o | o | o | o | o | o | ECR |
| 9 | 2 | o | o | o | o | o | o | o | o | "ECR, AR" |

Table 1 – Distribution of Electrodes within the Dataset

This figure represents the electrode placements and the seizure onset zones. Regions designated with "o" were available in the dataset, whereas those marked with "x" (*navy*) were not present. Abbreviations include: AHL, left hippocampal head; AHR, right hippocampal head; PHL, left hippocampal body; PHR, right hippocampal body; ECL, left entorhinal cortex; ECR, right entorhinal cortex; AL, left amygdala; AR, right amygdala; and SOZ symbolizes the seizure onset zone.

| Subject | AHL | AHR | PHL | PHR |
|---------|-----------------|-----------------|-----------------|-----------------|
| 1 | 0.60 ± 0.14 | n.a. | n.a. | 0.1 ± 0 |
| 2 | 0.21 ± 0.16 | 0.17 ± 0.21 | 0.18 ± 0.22 | 0.20 ± 0.15 |
| 3 | 0.40 ± 0.42 | 0.83 ± 0.12 | n.a. | n.a. |
| 4 | 0.10 ± 0.00 | 0.10 ± 0.00 | 0.90 ± 0.00 | 0.10 ± 0.14 |
| 5 | n.a. | n.a. | n.a. | n.a. |
| 6 | 0.63 ± 0.06 | n.a. | n.a. | 0.27 ± 0.06 |
| 7 | 0.10 ± 0.00 | 0.35 ± 0.35 | 0.37 ± 0.47 | 0.10 ± 0.00 |
| 8 | 0.13 ± 0.10 | n.a. | 0.28 ± 0.49 | n.a. |
| 9 | n.a. | 0.85 ± 0.07 | 0.15 ± 0.07 | n.a. |

Table 2 – Silhouette score of UMAP clustering for SWR^+ candidates and SWR^- candidates

The silhouette scores (mean \pm SD across sessions per subject) for UMAP clustering of SWR^+ candidates and SWR^- candidates (Figure 4A) were calculated based on their corresponding multiunit spike patterns (mean values were 0.205 [0.285], median [IQR]; Figure 4B).

| Subject ID | of sessions | of trials | ROI | of SWRs | SWR incidence [Hz] |
|------------|-------------|-----------------|-------------------------|---------|--------------------|
| 1 | 2 | 100 | AHL | 274 | 0.34 |
| 3 | 2 | 97 | AHR | 325 | 0.42 |
| 4 | 2 | 99 | PHL | 202 | 0.26 |
| 6 | 2 | 100 | AHL | 297 | 0.37 |
| 9 | 2 | 97 | AHR | 72 | 0.09 |
| Total = 10 | Total = 493 | "Total = 1,170" | 0.30 ± 0.13 (mean ± SD) | | |

Table 3 – Accounting for Defined SWR Events

The table collates statistics of putative CA1 regions and SWR events. Only the first two sessions (sessions 1 and 2) from each subject were considered to minimize sampling bias.

Figures

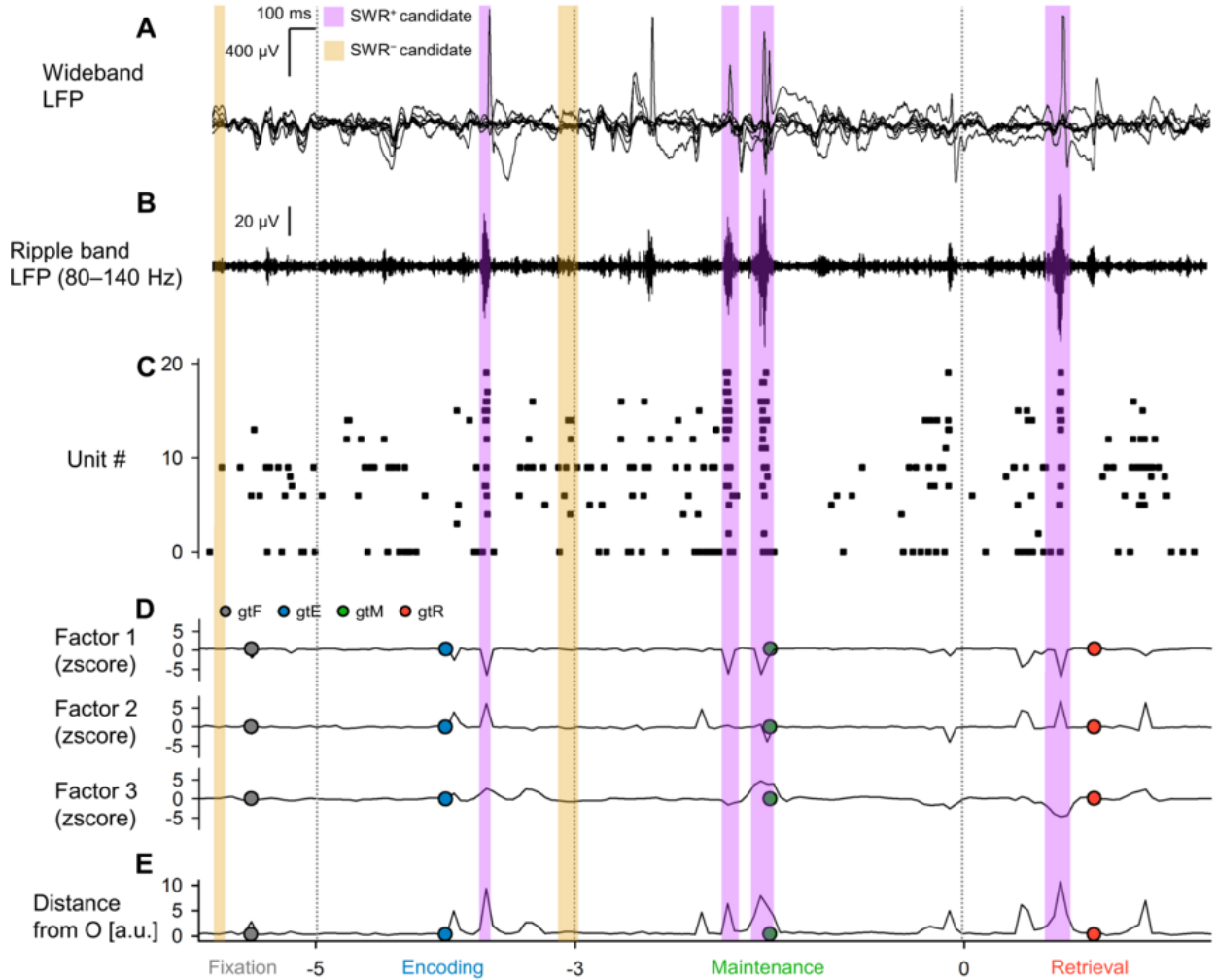


Figure 1 – Local Field Potentials (LFP), Multiunit Activity, and Neural Trajectories in the Hippocampus During a Modified Sternberg Task

A. These traces show representative wideband LFP intracranial EEG (iEEG) signals recorded from the left hippocampal head. The subject performed a modified Sternberg working memory task, which includes fixation (1 s, gray), encoding (2 s, blue), maintenance (3 s, green), and retrieval (2 s, red). **B.** We then present the corresponding ripple band LFP traces. **C.** The raster plot depicts multiunit spikes taken from the LFP traces, sorted using a spike algorithm [38]. **D.** Subsequently, we illustrate the neural trajectories, which are calculated by GPFA on spike counts per unit with 50-ms bins. Each phase's geometric median is marked by the dot circles. **E.** The trajectory's distance from the origin *O* is portrayed, with purple and yellow rectangles indicating the timings for SWR⁺ candidates and SWR⁻ candidates (considered as controls for SWR⁺), respectively.

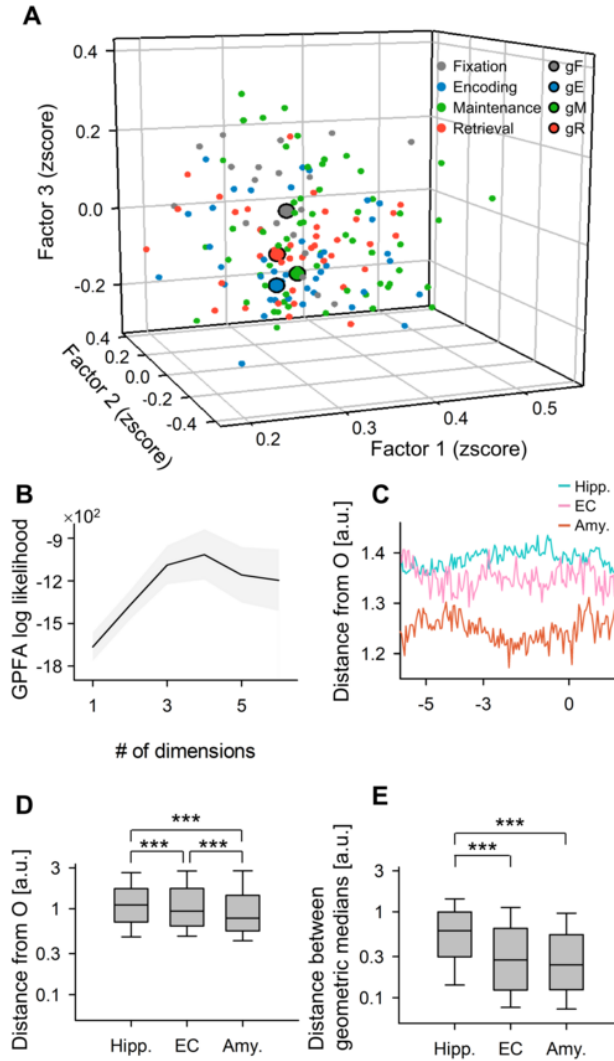


Figure 2 – State-Dependent Trajectories of Hippocampal Neurons

A. Neural trajectories within the initial three-dimensional factors derived from the Gaussian Process Factor Analysis (GPFA) are displayed. The smaller dots correspond to coordinates of 50-ms neural trajectory bins, while the larger dots with *black* edges signify the geometric medians for respective stages in the Sternberg working memory task: fixation (*gray*), encoding (*blue*), maintenance (*green*), and retrieval (*red*). **B.** The figure conveys the log-likelihood of the GPFA models versus the count of dimensions used to embed multiunit spikes found in the medial temporal lobe (MTL) territories. In specific, the elbow method pinpointed the optimal dimension to be three. **C.** This panel illustrates the distance of the neural trajectories from the origin (*O*) for the hippocampus (Hipp.), entorhinal cortex (EC), and amygdala (Amy.), against the time elapsed from the probe onset. **D.** The distance of the trajectory from *O* within MTL regions is displayed. The hippocampus shows the farthest distance, followed by the EC and the Amygdala. **E.** The plot represents inter-phase trajectory distances within the MTL regions. Abbreviations:

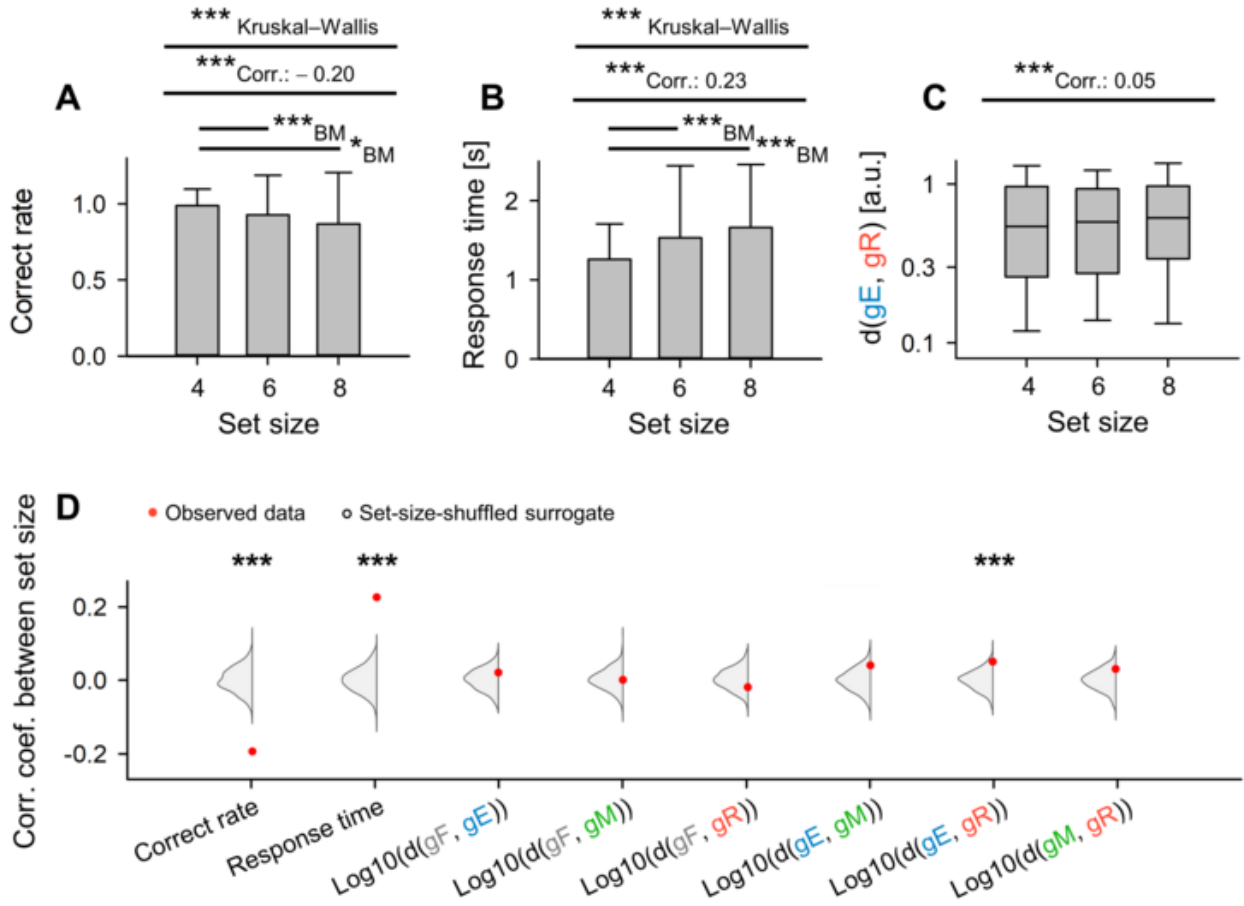


Figure 3 – Dependency of Trajectory Distance on Memory Load: Encoding and Retrieval States in Hippocampus

A. The relationship between set size (number of letters that need to be encoded) and correct rate in the working memory task (coefficient = -0.20, *** $p < 0.001$). **B.** The correlation between set size and response time (coefficient = 0.23, *** $p < 0.001$). **C.** The impact of set size on the inter-phase distances between the encoding and retrieval phases ($\|g_{EgR}\|$) (correlation coefficient = 0.05). **D.** Red dots represent experimental observations of correlations between set size and the following parameters: correct rate, response time, $\log_{10} \|g_{FgE}\|$, $\log_{10} \|g_{FgM}\|$, $\log_{10} \|g_{FgR}\|$, $\log_{10} \|g_{EgM}\|$, $\log_{10} \|g_{EgR}\|$, and $\log_{10} \|g_{MgR}\|$. The gray kernel density plot illustrates the corresponding set-size-shuffled surrogate ($n = 1,000$) (*** $ps < 0.001$).



Figure 4 – Detection of SWRs in Presumptive CA1 Regions

A. Two-dimensional UMAP (Uniform Manifold Approximation and Projection) [41] projection of multiunit spikes during SWR⁺ candidates (*purple*) and SWR⁻ candidates (*yellow*). **B.** Cumulative density plot shows silhouette scores, indicative of UMAP clustering quality, for hippocampal regions (see Table 2 for reference). Note that hippocampal regions with silhouette scores greater than 0.60 (equivalent to the 75th percentile) were identified as possible CA1 regions. SWR⁺ and SWR⁻ candidates recorded from these speculative CA1 regions were respectively classified as SWR⁺ and SWR⁻ (*ns* = 1,170). **C.** The identical distributions of durations are presented for SWR⁺ (*purple*) and SWR⁻ (*yellow*), owing to their definitions (93.0 [65.4] ms, median [IQR]). **D.** SWR incidence for both SWR⁺ (*purple*) and SWR⁻ (*yellow*) obtained relative to the probe's timing is illustrated as a mean \pm 95% confidence interval. However, as the intervals may not be visible due to their narrow range, note that a significant increase in SWR incidence was detected during the initial 400 ms of the retrieval phase (0.421 [Hz], **p* < 0.05, bootstrap test). **E.** The distributions of ripple band peak amplitudes for SWR⁻ (*yellow*; 2.37 [0.33] SD of baseline, median [IQR]) and SWR⁺ (*purple*; 3.05 [0.85] SD of baseline, median [IQR]) are delineated (****p* < 0.001, the Brunner–Munzel test).



Figure 5 – Transient Alterations in Neural Trajectory During SWR Events

A. Displayed is the distance from origin (*O*) of the peri-sharp-wave-ripple trajectory (mean \pm 95% confidence interval). The intervals may not be apparent due to their slender ranges. **B.** Shown is the distance from the origin (*O*) during pre-, mid-, and post-SWR periods (* p < 0.05, ** p < 0.01, *** p < 0.001; assessed using the Brunner–Munzel test). Abbreviations: SWR, sharp-wave ripple events; eSWR, SWR during the encoding phase; rSWR, SWR while in the retrieval phase; SWR⁺, positive SWR event; SWR⁻, control events for SWR⁺; pre-, mid-, or post-SWR denote the time intervals from –800 to –250 ms, from –250 to +250 ms, or from +250 to +800 ms, all relative to the center of the SWR.



Figure 6 – Visualization of Neural Trajectories during SWR in Two-Dimensional Spaces

The panels display hippocampal neural trajectories during SWR as projected onto two-dimensional spaces. **A.** Indicates hippocampal neural trajectories pre-SWR⁻ (gray), mid-SWR⁻ (yellow), and post-SWR⁻ (black). **B.** Represents the equivalents for SWR⁺ as opposed to SWR⁻. The $\|g_E g_R\|$ varied among sessions. The projection was applied in the following manner: First, a linear transformation positioned g_E at the origin O (0,0), and g_R at $(\|g_E g_R\|, 0)$. The point cloud was then rotated around the $g_E g_R$ axis (equivalent to the x axis) for fitting into two-dimensional spaces. Therefore, within these two-dimensional spaces, both the distances from O and the angles preserved the original makeup of the $g_E g_R$ axis from the original three-dimensional spaces. Abbreviations: SWR signifies sharp-wave ripple events; eSWR denotes SWR during the encoding phase; rSWR indicates SWR during the retrieval phase; SWR⁺, marks an SWR event; SWR⁻ refers to control events for SWR⁺; pre-SWR, mid-SWR, or post-SWR, reference the time intervals from -800 to -250 ms, from -250 to +250 ms, or from +250 to +800 ms from the center of SWR.

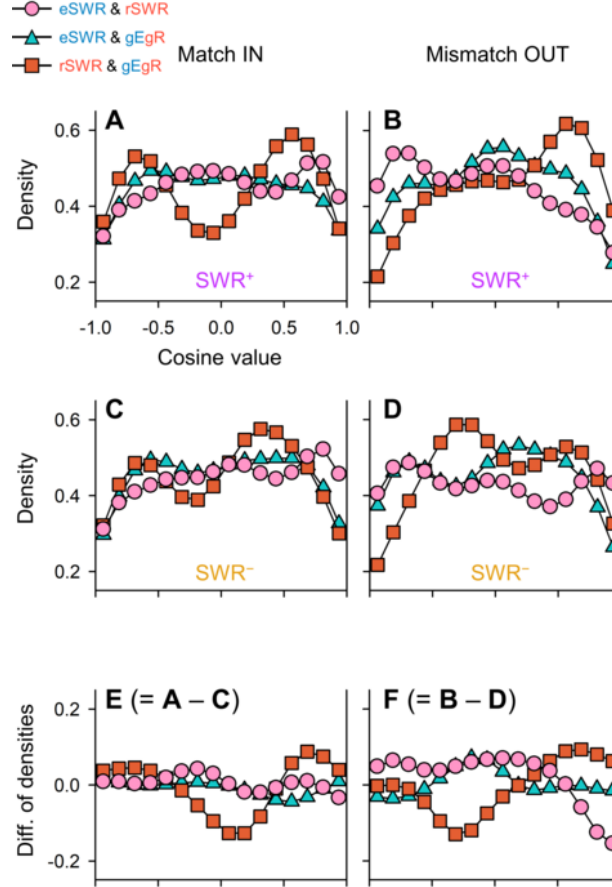


Figure 7 – Directions of Neural Trajectories during SWRs Based on Encoding and Retrieval States

A–B Kernel density estimation (KDE) distributions of $\overrightarrow{eSWR^+} \cdot \overrightarrow{rSWR^+}$ (pink circles), $\overrightarrow{eSWR^+} \cdot \overrightarrow{gEgR}$ (blue triangles), and $\overrightarrow{rSWR^+} \cdot \overrightarrow{gEgR}$ (red rectangles) in Match In (A) and Mismatch OUT tasks (B). **C–D** Present the corresponding distributions of SWR^- instead of those of SWR^+ in A and B. **E–F** Depict the differences in the distributions of SWR^+ and SWR^- , illuminating the SWR components ($E = C - A$; $F = D - B$). Note the biphasic distributions of $\overrightarrow{rSWR^+} \cdot \overrightarrow{gEgR}$, suggesting fluctuations between the encoding and retrieval states during the Sternberg task. Moreover, inverse directionality between $\overrightarrow{eSWR^+}$ and $\overrightarrow{rSWR^+}$ was observed (pink circles) in the Mismatch OUT task, but not in the Match IN task **E–F**). Finally, shifts from the retrieval to encoding states were evident in the SWR components in both the Match IN and Mismatch OUT tasks (red rectangles in E and F).